

## Research Article

# The Study of Dosimetric Characteristics of the XHA600D Medical Linear Accelerator Based on a Monte Carlo Code

Ningyu Wang <sup>1</sup>, Fengjie Cui,<sup>1</sup> Shaoxian Gu,<sup>1</sup> Chuou Yin,<sup>1</sup> Shengyuan Zhang,<sup>1</sup> Jinyou Hu,<sup>1,2</sup> Yunzhu Cai,<sup>1</sup> Zhangwen Wu,<sup>1</sup> Jun Wang,<sup>1</sup> and Chengjun Gou <sup>1</sup>

<sup>1</sup>Key Laboratory of Radiation Physics and Technology of Ministry of Education, Institute of Nuclear Science and Technology, Sichuan University, Chengdu 610064, China

<sup>2</sup>Cancer Center, Sichuan Academy of Medical Sciences & Sichuan Provincial People's Hospital, Chengdu 610072, China

Correspondence should be addressed to Chengjun Gou; goucjscu720@scu.edu.cn

Received 14 May 2022; Revised 19 July 2022; Accepted 22 August 2022; Published 29 September 2022

Academic Editor: Rafa Miró

Copyright © 2022 Ningyu Wang et al. This is an open access article distributed under the Creative Commons Attribution License, which permits unrestricted use, distribution, and reproduction in any medium, provided the original work is properly cited.

By investigating the influence of initial electrons on dosimetric characteristics, reasonable incident electron parameters for the nominal 6 MV photon beam of the XHA600D accelerator are finally established, i.e., a 6 MeV monoenergetic electron beam with a radial intensity FWHM of 2.5 mm and an angular divergency of 0.15°. Based on reasonable initial parameters, Percentage Depth Doses (PDDs), Off-Axis Ratios (OARs), total scatter factors, beam qualities, and penumbra widths of both flatteningfilter (FF) and flattening-filter-free (FFF) beams for fields ranging from 4 × 4 to 30 × 30 cm<sup>2</sup> are simulated systematically with EGSnrc codes. Not only the simulated dosimetric properties are in excellent agreement with the measurements, but also the dosimetric discrepancies between FF and FFF beams are consistent with the laws of previous studies on other accelerators. Therefore, reasonable incident electron parameters are able to accurately verify the performance of the XHA600D accelerator and can be used for further dosimetry research.

## 1. Introduction

Radiotherapy is one of the important means of oncotherapy, and the medical electron linear accelerator is the key equipment to realize the curative effect of tumor radiotherapy. Accurate acquisition of photon beam dosimetric characteristics (percentage depth dose or total scatter factor, for instance) of the accelerator is a pivotal step in quality assurance of radiotherapy, and these parameters are also the crucial data for the Treatment Planning System (TPS) to precisely calculate human dose distribution. Photons are generated from electrons impinging on a target, so accurate incident electron parameters (i.e., mean energy, energy spread, radial intensity distribution, and angular divergency) are further required for TPS model building. In general, Monte Carlo Codes [1, 2] are often used to simulate the accelerator head unit and initial electrons. Furthermore, the benchmarking procedures of electronic beams are carried out so that Percentage Depth Doses (PDDs), Off-Axis Ratios

(OARs), and other simulated properties are consistent with the measurements. These steps are ultimately designed to obtain the significant parameters in TPS model building. Many investigations have been conducted to benchmark the incident electrons of other medical linear accelerators such as Elekta [3–5], Varian [6–9], and Siemens [10, 11], but no dosimetric studies on the XHA600D accelerator have yet been found. And unlike these references, this study specifically analyzed the effects of these four incident electron parameters on PDDs and OARs in different beam fields and the details of the benchmarking process to obtain accurate incident electron information of the XHA600D accelerator.

In addition, the flattening filter in FF (flattening-filter) mode is used to produce an explanatory dose distribution. However, with the popularity of conformal radiotherapy technology, the necessity of flattening filters is greatly reduced. And numerous studies have demonstrated that FFF (flattening-filter-free) mode without the flattening filter has the advantages of increasing dose rate, improving treatment

efficiency, reducing the out-of-field dose, and heightening beam modeling accuracy [12]. Therefore, FFF mode has been widely used in clinical treatment, especially for high-dose stereotactic body radiation therapy (SBRT).

Therefore, based on these differences between FF and FFF beams, the dosimetric characteristics of the 6 MV XHA600D accelerator in two modes were systematically simulated and compared with the experimental data after obtaining reasonable incident electron parameters. Many other studies (such as Bencheikh et al. [6]) only compared experimental and simulated PDD and OAR data based on the incident electron parameters and did not analyze the FF and FFF modes separately. In addition to researching the incident electron parameters, this study has taken a more comprehensive approach with Monte Carlo codes to verify the performance of the XHA600D accelerator from two aspects. The first one is that the simulated data should be able to reproduce the experimental dose distribution to a certain level of accuracy, and the second one is that the dosimetric difference between FF mode and FFF mode should be in accordance with the conclusions obtained by previous studies [12–14]. And this study confirmed the agreement between measured and simulated data from multiple parameters (such as percentage depth dose, off-axis ratio, total scatter factor, beam quality, penumbra width, flatness, and symmetry).

## 2. Materials and Methods

**2.1. Measurement of Photon Beam Dosimetric Parameters.** The dosimetric parameters of the accelerator required in this study were measured by the manufacturer with a Blue Phantom2- 3D and a DOSE1 dosimeter (IBA Dosimetry, Belgium). The scanning volume of the water phantom is  $478 \times 478 \times 410 \text{ mm}^3$  ( $X/Y/Z$ ). Under the condition that source to surface distance (SSD) is equal to 100 cm, the off-axis doses and central axis depth doses for eight different fields of  $4 \times 4$ ,  $6 \times 6$ ,  $8 \times 8$ ,  $10 \times 10$ ,  $15 \times 15$ ,  $20 \times 20$ ,  $25 \times 25$ ,  $30 \times 30 \text{ cm}^2$  were measured, and the measurement step length was 1 mm. The measurements of off-axis doses were conducted at various depths, which are  $d_{\text{max}}$ , 5, 10, 20, 25 cm for FF beams and  $d_{\text{max}}$ , 5, 10, 20, 30 cm for FFF beams, respectively. In addition, the PTW 30013 farmer ionization chamber (PTW, Freiburg, Germany) was applied to measure total scatter factor. The measurement indicators of the above detection instruments obviously exceed the standards of IEC 60731 and AAPM. All experimental data in this study were professionally measured by the accelerator manufacturer, and the statistical uncertainties of the measured dose values were generally less than 1% (coverage factor  $k=2$ ).

**2.2. Monte Carlo Codes and Parameters.** Using EGSnrc user codes [15], the MC simulations were performed based on a System HP Pavilion 500–151 in server consisting of an Intel (R) Core (TM) i5-4570 CPU (3.2 GHz each) and RAM of 8 GB. The Monte Carlo simulations were divided into two steps. According to hardware parameters information of the accelerator head provided by the manufacturer, the first

stage was to simulate the 6 MV FF beams and FFF beams of the XHA600D accelerator with the BEAMnrc user code [16] of the Monte Carlo-based EGSnrc code system. In this study, different components of the treatment head were modeled, including the target, primary collimator, flattening filter, ion chamber, mirror, and secondary collimator. Figure 1 shows the FF beam mode of the linear accelerator simulated by BEAMnrc user code. When simulating FFF beam mode, the flattening filter was replaced with 0.3 cm-thick aluminum foil. All materials used in the Monte Carlo simulation were extracted from the 700 ICRU PEGS4 (pre-processor for Electron Gamma Shower) cross-section data.

In the BEAMnrc simulations, the electron cutoff energy (ECUT) and photon cutoff energy (PCUT) values were set to 0.7 and 0.01 MeV, respectively. Range rejection [17] was turned on with an ESAVE value (maximum electron energy at which range rejection is considered) of 1 MeV in the target and 2 MeV in other components. The maximum CPU hours allowed is 1000 hours. Directional bremsstrahlung splitting (DBS) [18], the variance reduction technique, was adopted during BEAMnrc simulation to improve the calculation efficiency. The bremsstrahlung splitting number (NBRSP) was set to 1000 and the splitting radius was equal to the corresponding field size. Different initial electron histories were set for different field sizes, and the adjustment range was  $6 \times 10^8 \sim 1 \times 10^9$ . Combined with the above simulation parameters, the Gaussian distribution source (ISOURC = 19 Elliptical Beam with Gaussian Distributions in  $X$  and  $Y$ , Parallel or with Radial Divergence) was selected to estimate the incident electron parameters. The user interface for the Gaussian distribution source is shown in Figure 2. At a distance of 100 cm from the target, a phase space plane was set to record the particles generated by the BEAMnrc code. The main EGSnrc transport parameters are listed in Table 1.

In the second step, the phase space file derived from the above BEAMnrc code was input into the DOSXYZnrc code [19], and it was placed on the surface of a  $50 \times 50 \times 50 \text{ cm}^3$  water phantom as a source. The voxel dimension of the water phantom was  $0.2 \times 0.2 \times 0.2 \text{ cm}^3$ . The central axis depth doses and the lateral profiles in the  $X$  directions at various depths ( $d_{\text{max}}$ , 5, 10, 20, and 25 cm for FF beams and  $d_{\text{max}}$ , 5, 10, 20, and 30 cm for FFF beams) were recorded respectively.  $1 \times 10^9$  particle histories were initiated in the DOSXYZnrc simulation. The statistical uncertainties with regard to the absorbed dose values in the calculation were expressed with the condition of “coverage factor  $k=2$ .”

**2.3. Data Comparison and Analysis.** In this study, an algorithm for gamma passing rates [20], which was used to compare simulated and measured dose distributions, was written with MATLAB software. Generally, the evaluation of the  $\gamma$  index was performed by the algorithms of Dose Difference (DD) and Distance-To-Agreement (DTA) in a complementary manner. The passing criterion was considered when the  $\gamma$  index was equal to or less than 1.

In order to ensure the same monitor units (MUs), total scatter factors ( $S_{c,p}$ ) were gained with the following method. The dose of  $10 \times 10 \text{ cm}^2$  field at the ion chamber was,  $D_{10}^C$ ,

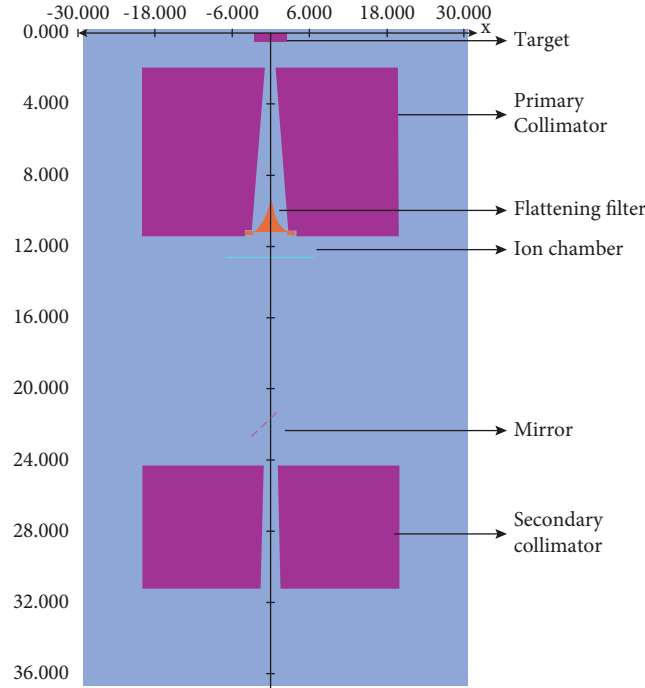


FIGURE 1: Detailed treatment head structure of XHA600D medical linear accelerator. The units of the numbers on the axes are “cm.” From top to bottom, the components are, in order, target, primary collimator, flattening filter, ion chamber, mirror, and secondary collimator. Phase space files are generated on the scoring plane at  $z = 100$  cm.

and the dose of other fields at the ion chamber was set as  $D_n^C$ . expressed by  $k = D_{10}^C / D_n^C$ , and total scatter factor can be

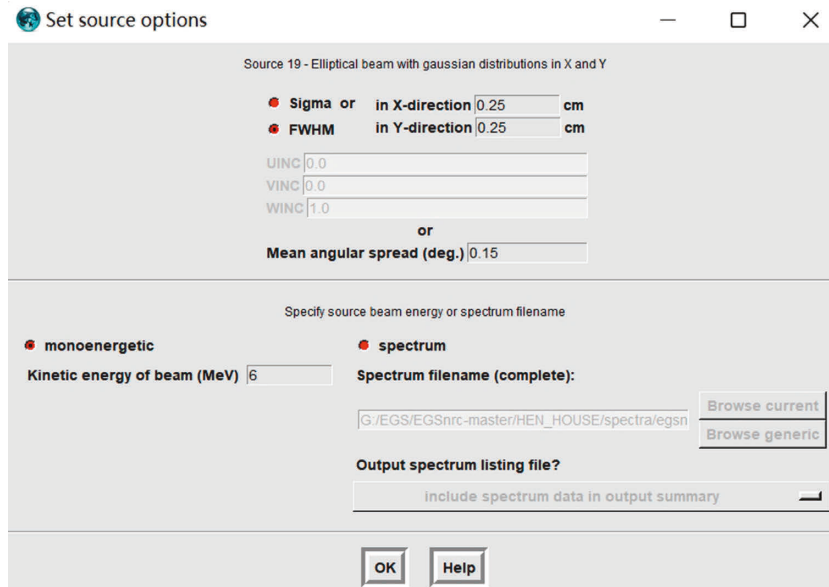


FIGURE 2: The Gaussian distribution source (ISOURC = 19) parameter settings in the BEAMnrc code.

The dose of  $10 \times 10$  cm<sup>2</sup> field at the maximum dose depth on the central axis of the water phantom was,  $D_{10}$ , and the dose of other fields at the same point in the water phantom was,  $D_n$ . The doses at ion chamber of different fields were treated as equal, i.e.,  $D_{10}^C = kD_n^C$ . Hence, coefficient  $k$  can be,

defined from the following relation:

$$S_{c,p} = \frac{k \times D_n}{D_{10}} = \frac{D_{10}^C \times D_n}{D_n^C \times D_{10}} \tag{1}$$

TABLE 1: The main EGSnrc transport parameters used in this study.

EGSnrc transport parameters	Value
Maximum step size (SMAX)	5 cm
Maximum fractional energy loss/step (ESTEPE)	0.25
Maximum first elastic scattering moment per step (XIMAX)	0.5
Boundary crossing algorithm	EXACT
Electron-step algorithm	PRESTA-II
Brems angular sampling	KM
Brems cross sections	BH
Bound compton scattering	Norej
Compton cross sections	Default
Pair angular sampling	Simple
Pair cross sections	BH

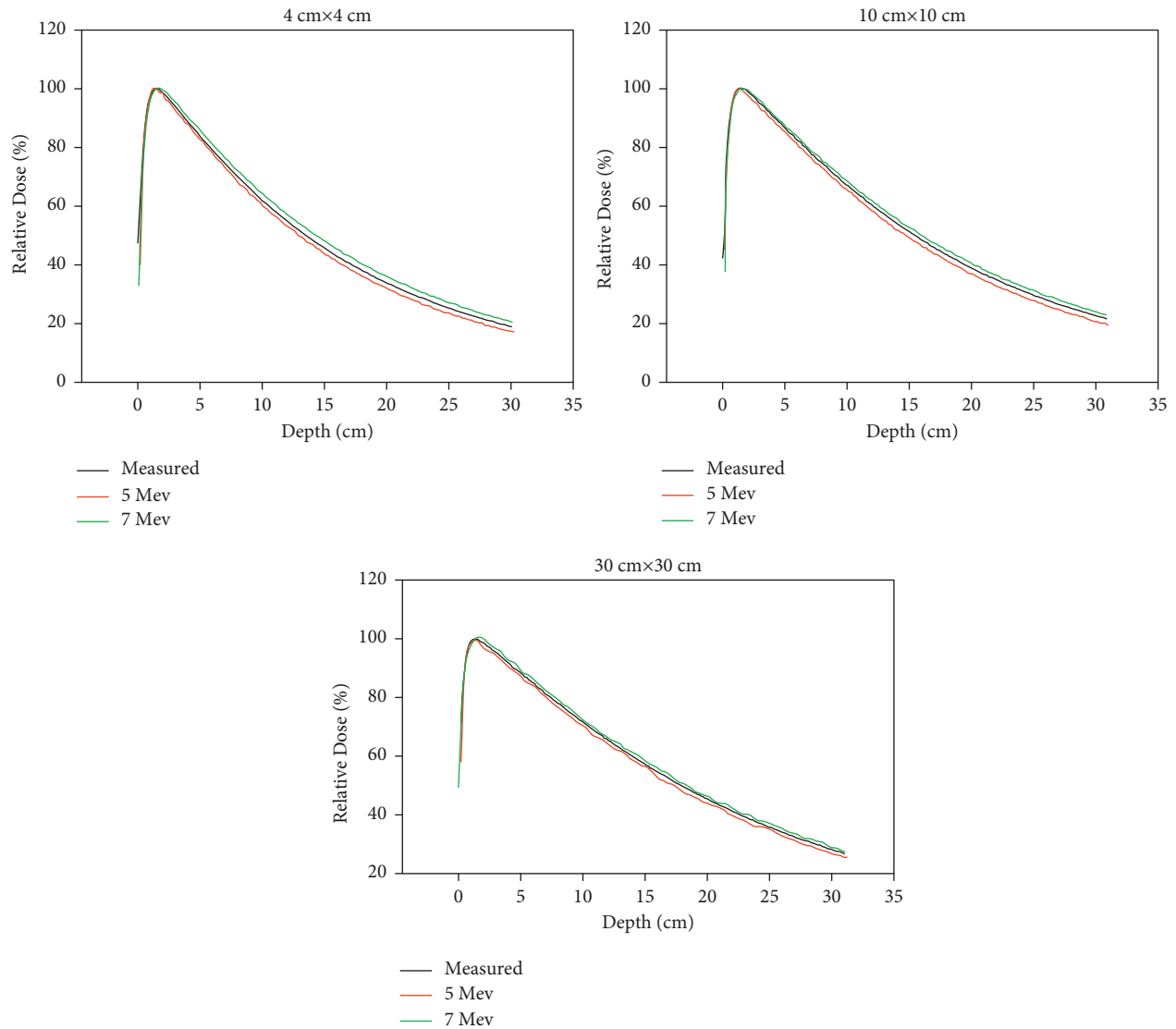


FIGURE 3: The influence of mean energy of incident electron on PDDs for  $4 \times 4$ ,  $10 \times 10$ ,  $30 \times 30$  cm<sup>2</sup> fields. Red curve represents the dose curve when the energy is 5 MeV, the green curve represents the dose curve when the energy is 7 MeV, and the black curve represents the measured dose curve.

The conventional definition of penumbra width is the distance between the positions of 80% and 20% of the central axis, but this method applies only to FF beams, and is no

longer suitable for FFF beams. Therefore, the renormalization method [21] recommended by Fogliata et al. was used to analyze the penumbra in this study. Before calculating the

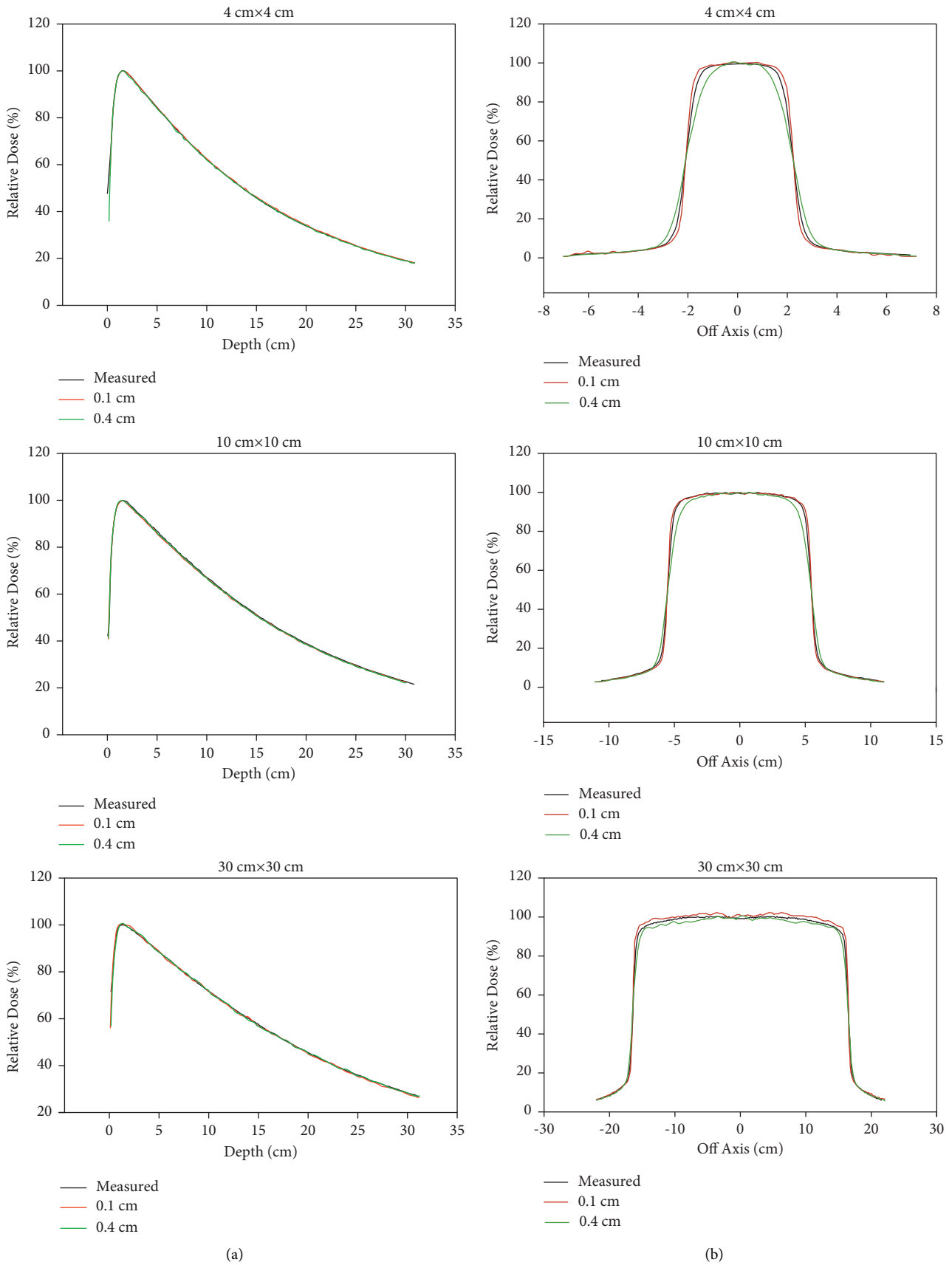


FIGURE 4: (a) The influence of the radial intensity distribution of incident electrons on PDDs for 4×4, 10×10, 30×30 cm<sup>2</sup> fields. (b) The influence of radial intensity distribution of incident electron on OARs for 4×4, 10×10, 30×30 cm<sup>2</sup> fields at 10 cm depth. The red curve represents the dose curve when the radial intensity FWHM is 0.1 cm, the green curve represents the dose curve when the radial intensity FWHM is 0.4 cm, and the black curve represents the measured dose curve.

TABLE 2: The comparison of simulated and measured penumbra widths (cm) at 0.1, 0.25, and 0.4 cm for three different fields at 10 cm depth. The uncertainties of simulated values were less than or equal to 2% under the condition of  $k = 2$ .

FWHM (cm) of three field sizes	Penumbra widths		
	Simulated (cm)	Measured (cm)	Diff. (%)
0.1 ( $4 \times 4 \text{ cm}^2$ )	0.410	0.649	-36.8
0.25 ( $4 \times 4 \text{ cm}^2$ )	0.646	0.649	-0.462
0.4 ( $4 \times 4 \text{ cm}^2$ )	0.977	0.649	50.5
0.1 ( $10 \times 10 \text{ cm}^2$ )	0.539	0.752	-28.3
0.25 ( $10 \times 10 \text{ cm}^2$ )	0.748	0.752	-0.532
0.4 ( $10 \times 10 \text{ cm}^2$ )	1.20	0.752	59.6
0.1 ( $30 \times 30 \text{ cm}^2$ )	0.551	0.991	-44.4
0.25 ( $30 \times 30 \text{ cm}^2$ )	0.990	0.991	-0.101
0.4 ( $30 \times 30 \text{ cm}^2$ )	1.25	0.991	26.1

penumbra widths of FFF beams, the off-axis dose curves of FFF beams were renormalized. Then the points of 80% and 20% dose values on the renormalized beam profiles were extracted. In this study, the measurements of each field at 10 cm depth were compared with the simulated penumbras.

Flatness and symmetry are two significant dosimetric indicators, which are bound to directly affect the effectiveness of radiation therapy. Beam flatness was assessed by looking for the maximum dose  $D_{\max}$  and the minimum dose  $D_{\min}$  within 80% of the central field width at a depth of 10 cm in the water phantom. The computation of flatness ( $F$ ) was implemented using the following formula:

$$F = \frac{D_{\max} - D_{\min}}{D_{\max} + D_{\min}}. \quad (2)$$

Symmetry can be described as the difference between the dose rates of two points which deviate symmetrically from the central axis within 80% of field width divided by the dose rate at the central axis. In this research, the dose at 80% of field width was taken to assess symmetry.

The beam quality was characterized by the tissue phantom ratio  $\text{TPR}_{20,10}$  [22], that is,

$$\text{TPR}_{20,10} = 1.2661\text{PDD}_{20,10} - 0.0595, \quad (3)$$

where  $\text{PDD}_{20,10}$  is the ratio of the percent depth doses at 20 and 10 cm depths for  $10 \times 10 \text{ cm}^2$  field when SSD is equal to 100 cm.

### 3. Results and Discussion

*3.1. Reasonable Estimation of Incident Electron Parameters.* The accuracy of the incident electron beam plays a vital role in the Monte Carlo simulation of accelerator photons, and the variations of incident electron parameters have a great influence on dose distribution. Nevertheless, it is time-consuming to modulate and test incident electron beam parameters on a larger scale. In our previous study [23], we discussed a benchmarking process for incident electron parameters of the XHA600D accelerator in the case of  $10 \times 10 \text{ cm}^2$  field. We supplemented the previous research by selecting three cases of  $4 \times 4$ ,  $10 \times 10$  and  $30 \times 30 \text{ cm}^2$  that can represent small, reference and large fields, and investigated the effects of different incident parameters on dose

distribution PDDs and OARs in FF mode. In this study, the optimal combination of incident electron parameters was determined by independent analysis of mean energy, energy spread, radial intensity distribution, and angular divergency. And the uncertainties of all simulated dose distribution were less than or equal to 2% under the condition of  $k = 2$ .

The first was the determination of mean energy. AlMBERG et al. [4] and Lin et al. [24] show that the mean energy of the incident electron beam has a great influence on the PDD and OAR curve. While the PDD curve is mainly affected by the energy of the incident electron beam, this conclusion can also be drawn from the analysis of the influence of the following three parameters on PDDs. Thus, the mean energy can be determined by comparing simulated and measured PDDs. When the other three parameters remain unchanged, Figure 3 shows the influence of mean energy with a minimum value of 5 MeV and a maximum value of 7 MeV on PDDs under different beam fields. It can be seen that when the energy is 7 MeV, the simulated dose after the maximum dose depth is higher than the measured dose. And when the energy is 5 MeV, the simulated dose after the maximum dose depth is lower than the measured dose. Therefore, it is found that when the mean energy is 6 MeV, the simulated PDDs and the measured PDDs meet the Gamma criteria of 1 mm/1% (local dose) through adjustment.

The second is the determination of the radial intensity distribution. When the other three parameters remain unchanged, Figure 4(a) shows the influence of radial intensity FWHM with a minimum value of 0.1 cm and a maximum value of 0.4 cm on PDDs under different beam fields. It can be seen that the radial intensity distribution of incident electrons has little influence on the PDDs for  $4 \times 4$ ,  $10 \times 10$ ,  $30 \times 30 \text{ cm}^2$  fields. Figure 4(b) shows the influence of radial intensity FWHM with a minimum value of 0.1 cm and a maximum value of 0.4 cm on OARs under different beam fields at 10 cm depth. When FWHM increases, the penumbra area of the OAR curve becomes oblique and the penumbra width increases obviously, which is more obvious in the case of a small field. Therefore, the accurate radial intensity distribution of incident electrons can be determined by making the difference between simulated and measured penumbra widths less than 1%. Table 2 shows the comparison of simulated and measured penumbra widths at 0.1, 0.25, and 0.4 cm for three different fields at 10 cm depth

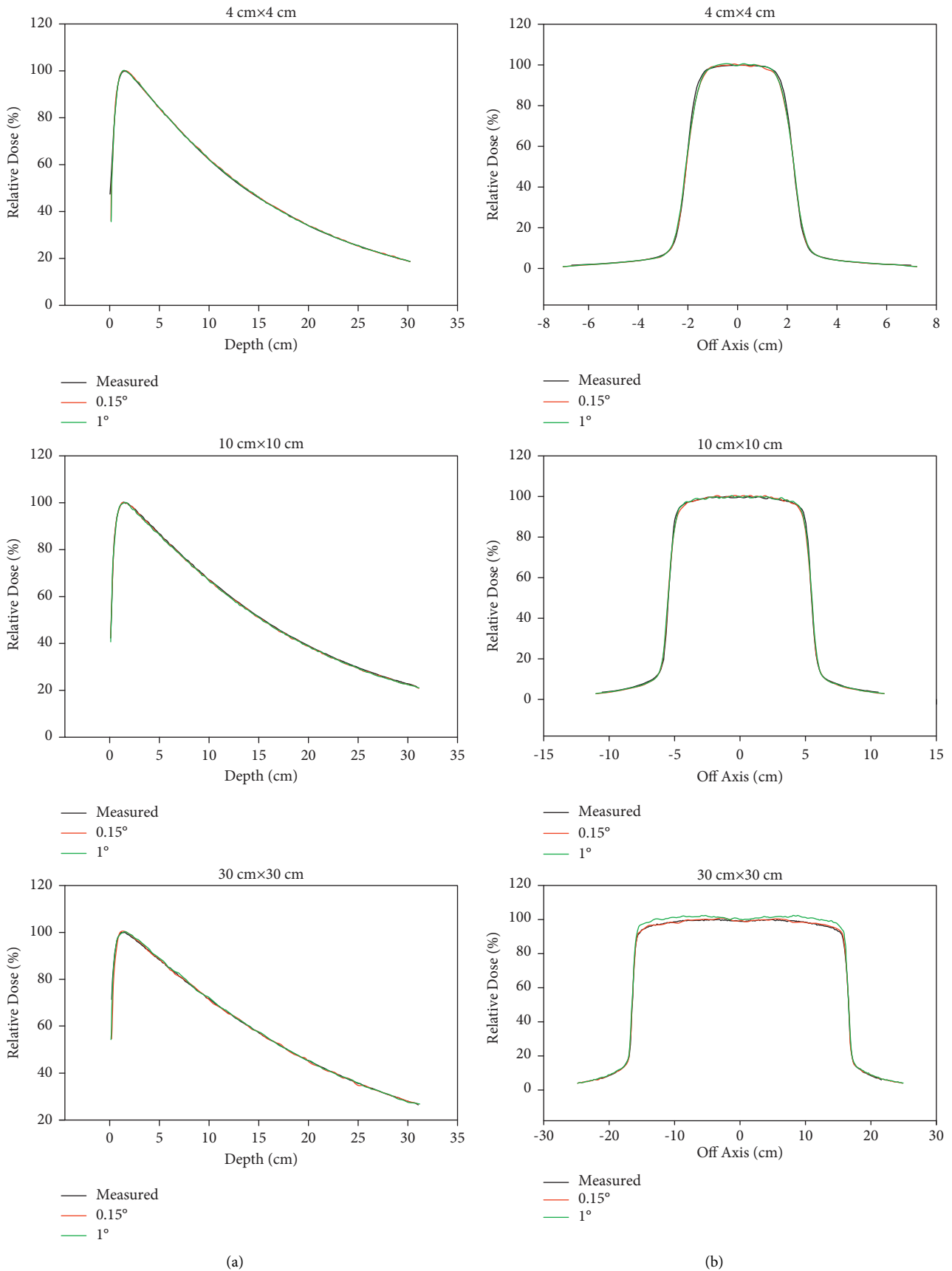


FIGURE 5: (a) The influence of the angular divergency of incident electrons on PDDs for 4 × 4, 10 × 10, 30 × 30 cm<sup>2</sup> fields. (b) The influence of angular divergency of incident electron on OARs for 4 × 4, 10 × 10, 30 × 30 cm<sup>2</sup> fields at 10 cm depth. The red curve represents the dose curve when the angular divergency is 0.15°, the green curve represents the dose curve when the angular divergency is 1°, and the black curve represents the measured dose curve.

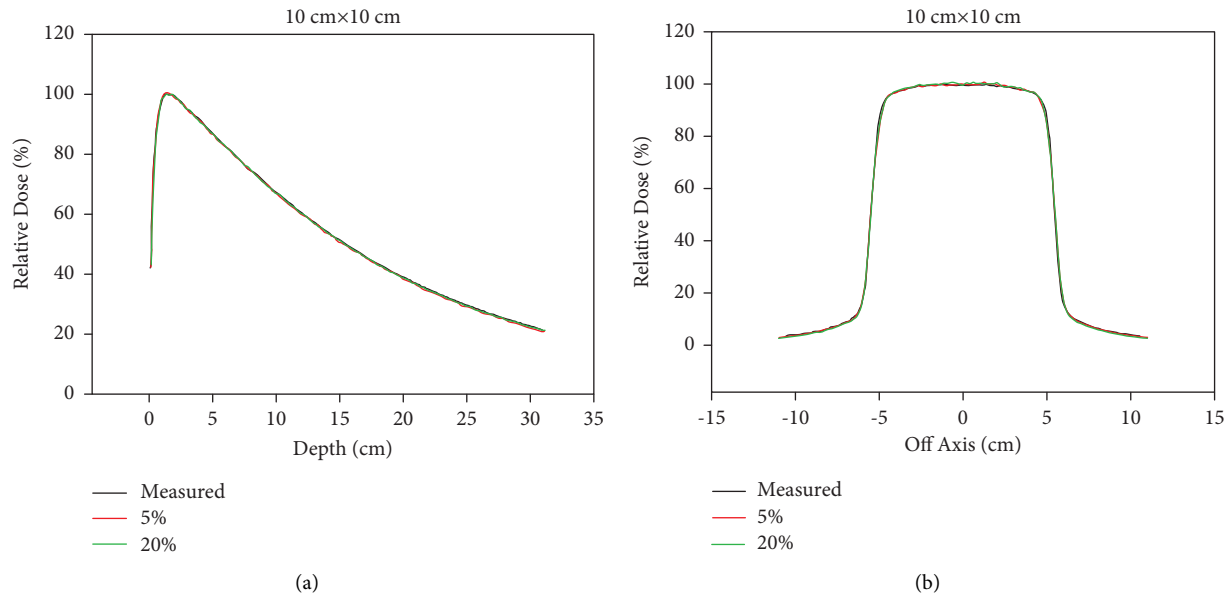


FIGURE 6: (a) The influence of the energy spread of incident electrons on PDDs for  $10 \times 10 \text{ cm}^2$  field. (b) The influence of energy spread of incident electron on OARs for  $10 \times 10 \text{ cm}^2$  field at 10 cm depth. Red curve represents the dose curve when the energy spread is 5%, the green curve represents the dose curve when the angular divergency is 20%, and the black curve represents the measured dose curve.

(the uncertainties of simulated values were less than or equal to 2% under the condition of  $k=2$ ). It can be seen from Table 2 that when  $\text{FWHM} = 0.25 \text{ cm}$ , the simulation results are highly consistent with the measurement results.

The third is the determination of angular divergence. When the other three parameters remain unchanged, Figure 5(a) shows the influence of angular divergency with a minimum value of  $0.15^\circ$  and a maximum value of  $1^\circ$  on PDDs under different beam fields. It can be seen that the angular divergency of incident electrons has little influence on the PDDs for  $4 \times 4$ ,  $10 \times 10$ ,  $30 \times 30 \text{ cm}^2$  fields. Figure 5(b) shows the influence of angular divergency with a minimum value of  $0.15^\circ$  and a maximum value of  $1^\circ$  on OARs under different beam fields at 10 cm depth. It can be seen that the OAR curve is not sensitive to the angular divergency in the case of a small field. However, for larger fields, when the angular divergency increases, the central area of the OAR curve, especially the shoulder, becomes higher. And the outer penumbra area does not change significantly. In addition, it can be seen from the figure that the simulated OAR curve is in good agreement with the measured OAR curve when the angular divergency is  $0.15^\circ$ , and the Gamma criteria of 1 mm/1% (local dose) were met in three different fields.

The fourth is the determination of energy spread. It is assumed that energy spread is of the same type as the radial intensity distribution, which is the Gaussian distribution. Energy spread is expressed as a percentage, which is equal to the ratio of the FWHM of the Gaussian spectrum to the mean energy. It is found that the PDD and OAR curves do not change significantly when the energy spread is 5% at the minimum and 20% at the maximum. We only show the effect of energy spread on dose distribution in the case of  $10 \times 10 \text{ cm}^2$  field in

Figure 6. Therefore, in the simulation, the energy spread of incident electrons can be set to 0%.

A 6 MeV monoenergetic electron beam with a radial intensity FWHM of 2.5 mm and an angular spread of  $0.15^\circ$  was finally determined as a reasonable incident electron, which is applicable to both the FF and FFF modes of the XHA600D accelerator. After determining reasonable incident electron characteristics, PDDs and OARs for eight different fields of  $4 \times 4$ ,  $6 \times 6$ ,  $8 \times 8$ ,  $10 \times 10$ ,  $15 \times 15$ ,  $20 \times 20$ ,  $25 \times 25$ ,  $30 \times 30 \text{ cm}^2$  were systematically calculated, and the dosimetric properties of both the FF and FFF beam-modes were further analyzed and demonstrated.

### 3.2. Comparative Analysis of Simulation and Measurement

**3.2.1. Percentage Depth-Dose Characteristics.** PDDs were calculated for 6 MV FF and FFF beams for the field sizes of  $4 \times 4$ ,  $6 \times 6$ ,  $8 \times 8$ ,  $10 \times 10$ ,  $15 \times 15$ ,  $20 \times 20$ ,  $25 \times 25$ ,  $30 \times 30 \text{ cm}^2$ . Both the calculated and measured depth dose curves were normalized to the depth of maximum dose and then compared. The statistical uncertainties of calculated depth doses were between 0.1 and 1% (coverage factor  $k=2$ ). For the sake of clarity, they are not shown in figures. The simulated and measured PDDs for various field sizes are plotted in Figure 7, in which solid lines represent measured data and dotted lines represent simulated data. Figure 7(a) shows the percentage depth-dose curves of 6 MV FF beams, and Figure 7(b) shows the percentage depth-dose curves of 6 MV FFF beams. For all the fields in this study, gamma criteria of 1 mm/1% (local dose) can be met for the comparison between the calculated and measured PDDs. Furthermore, simulated PDD curves formed by FF beam and FFF beam in  $10 \times 10 \text{ cm}^2$  field were compared in Figure 8,

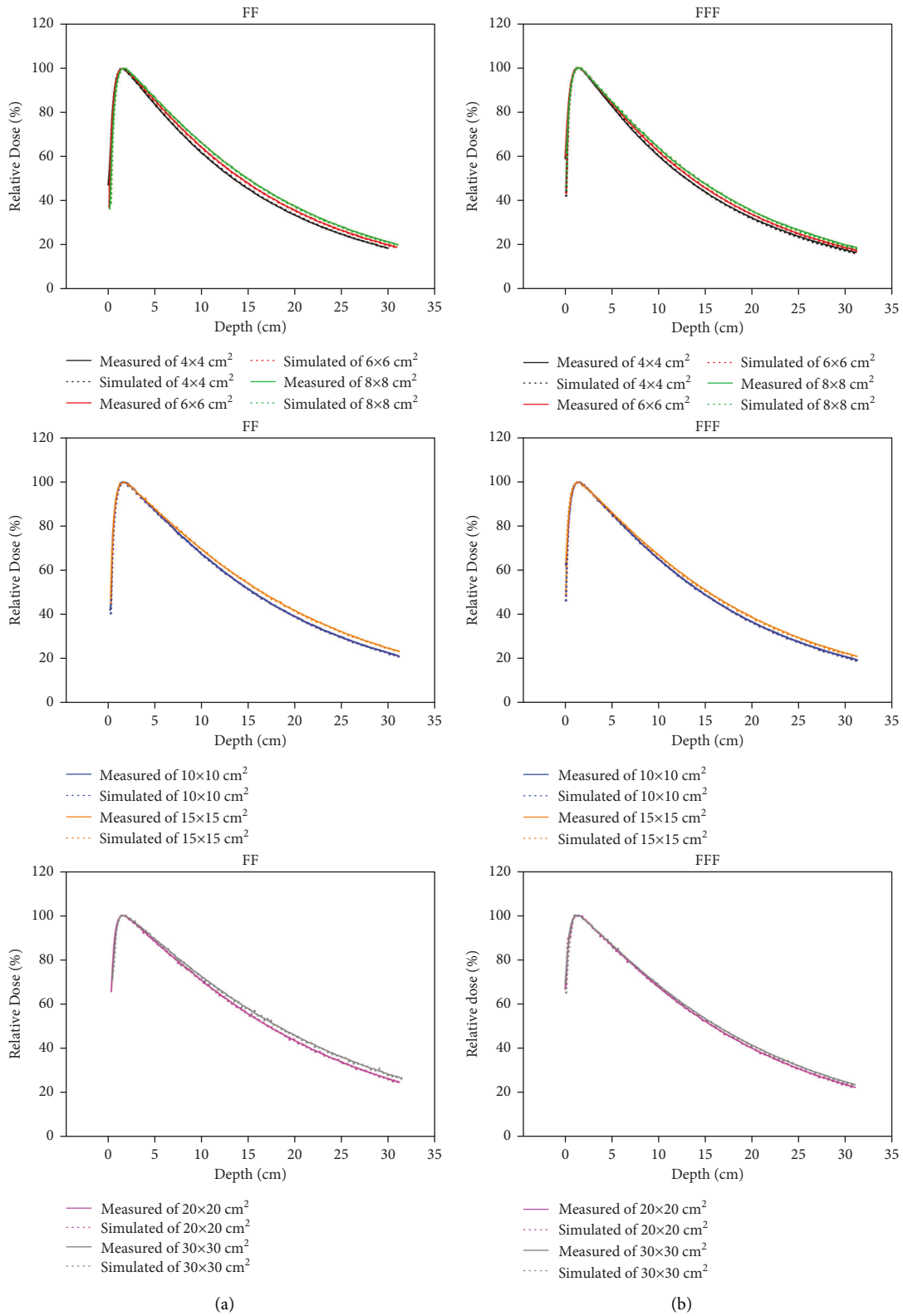


FIGURE 7: (a) The comparison of measured and simulated PDDs for various field sizes ( $\text{cm}^2$ ) of 6 MV FF beams. (b) The comparison of measured and simulated PDDs for various field sizes ( $\text{cm}^2$ ) of 6 MV FFF beams. All curves are normalized to the depth of the respective maximum dose. In order to show the contrast more clearly, the seven fields are split into three panels.  $4 \times 4$ ,  $6 \times 6$ ,  $8 \times 8$ ,  $10 \times 10$ ,  $15 \times 15$ ,  $20 \times 20$ ,  $30 \times 30 \text{ cm}^2$  fields are shown in order by black, red, green, blue, orange, pink, and gray curves. Solid lines represent measured data and dotted lines represent simulated data.

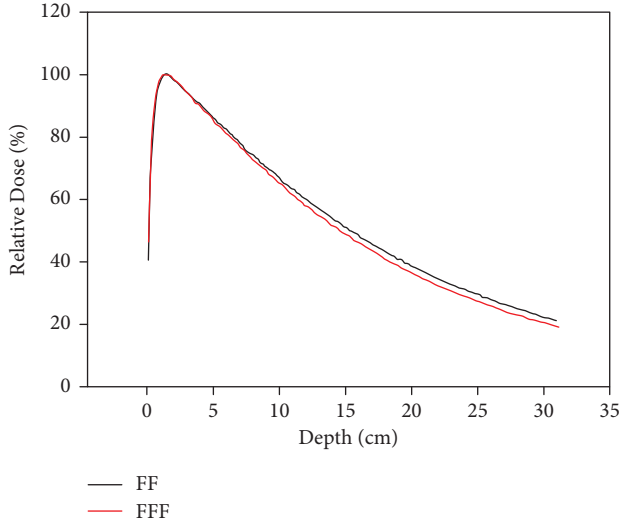


FIGURE 8: The comparison of simulated PDDs formed by FF beam and FFF beam for  $10 \times 10 \text{ cm}^2$  field. The black line represents the FF beam result and the red line represents the FFF beam result.

TABLE 3: The simulated and measured beam qualities of the FF beam and FFF beam are shown. The uncertainties of the simulated beam qualities of FF and FFF beam were 0.6% and 0.7% (coverage factor  $k=2$ ), respectively.

Beam	Simulated	$TPR_{20,10}$	
		Measured	Diff. (%)
FF	0.681	0.677	0.590
FFF	0.653	0.652	0.153

which served to show that the central axis dose formed by FFF beam, with the removal of flattening filter, was lower. Furthermore, this difference became more pronounced with the increase in depth. The gradually shallow PDD curves are due to the fact that FFF beams do not undergo hardening in flattening filters and the photon energy spectrums soften. This point can also be reflected in the investigation of beam quality.

**3.2.2. Beam Quality  $TPR_{20,10}$ .** The beam qualities of 6 MV FF and FFF beams are listed in Table 3, which shows that the differences between the simulated and measured tissue phantom ratios are less than 0.6% for both beams. Moreover, the beam quality of the 6 MV FFF beam was smaller than that of the 6 MV FF beam, indicating that the removal of the flattening filter makes the beam quality softer. In agreement with the analyses of dosimetric properties of Elekta Precise linac from Georg et al. [25], FFF beams revealed steeper dose reductions at depths greater than the maximum dose.

**3.2.3. Off-Axis Dose Distribution and Gamma Analysis.** The simulated and measured off-axis dose distributions in eight different fields, ranging from  $4 \times 4$  to  $30 \times 30 \text{ cm}^2$ , were compared. The statistical uncertainties of calculated off-axis

doses were mostly below 0.6% (coverage factor  $k=2$ ) and about 1.6% for regions near the field edge. Both FF mode and FFF mode showed excellent conformance. For convenience, only the off-axis dose curves for three cases of minimum field, maximum field, and reference field were presented in this paper. The comparisons of the measured and simulated off-axis dose curves of 6 MV FF beams for  $4 \times 4$ ,  $10 \times 10$ ,  $30 \times 30 \text{ cm}^2$  field sizes at various depths ( $d_{\max}$ , 5, 10, 20, 25 cm) are plotted in Figure 9(a), and similar comparison of 6 MV FFF beams at various depths ( $d_{\max}$ , 5, 10, 20, 30 cm) are plotted in Figure 9(b). The OARs of both FF and FFF beams were normalized according to the central axis depth doses that correspond to respective depths. The comparison of the off-axis doses displayed that the simulations could reproduce the measurements well in the case of reasonable incident electrons.

Gamma analyses of off-axis dose distributions for different fields at 10 cm depth were introduced to clearly characterize the degree of matching. For all field sizes of FF and FFF beams, the criteria containing Distance-To-Agreement and Dose Difference of 2 mm/1% can be fulfilled. Under the restriction of 1 mm/1% (Local Dose), apart from the fields larger than  $20 \times 20 \text{ cm}^2$  of FF beams and the fields larger than  $25 \times 25 \text{ cm}^2$  of FFF beams, the gamma passing rates of calculated and measured OARs for other fields were 100%, which is shown in Table 4.

There were two possible reasons accountable for these: first, as the field size increases, the deviation of off-axis dose increases relatively; second, the penumbra region is a high-dose gradient region, which has a larger deviation than the regions within the beam field.

The gamma analysis results of measured and simulated OARs for a  $10 \times 10 \text{ cm}^2$  field at 10 cm depth are shown in Figure 10. These two figures plot the gamma curves corresponding to the difference of simulated and measured off-axis doses generated by FF and FFF beams. The agreement was within 1 mm/1% in both two cases.

**3.2.4. Penumbra Width.** Table 5 presents the comparison of MC-calculated and measured penumbra widths at 10 cm depth for diverse field sizes. As can be seen from the table, the penumbra disparity between calculations and measurements for all fields of FF and FFF beams was 0.039 cm at the maximum and 0.001 cm at the minimum. Compared with the FF beam mode, the penumbra region of the FFF beam had a more precipitous descending tendency [12].

**3.2.5. Total Scatter Factor.** The contrasts of measured and calculated total scatter factors were performed at  $SSD=100 \text{ cm}$  and a depth equal to  $d_{\max}$  for various field sizes. The data for two situations with and without flattening filter are exhibited in Table 6. As shown in Table 6, the simulated  $S_{c,p}$  values agreed well with the measured values for various fields (the differences were less than 1%). Meanwhile,  $S_{c,p}$  values of both beams increased with the enlargement of the field size, but the increase amplitude of  $S_{c,p}$  for FFF beams was smaller than that for FF beams, because the scattering of treatment head is reduced after removing the flattening filter. For FF beams, the ratio of

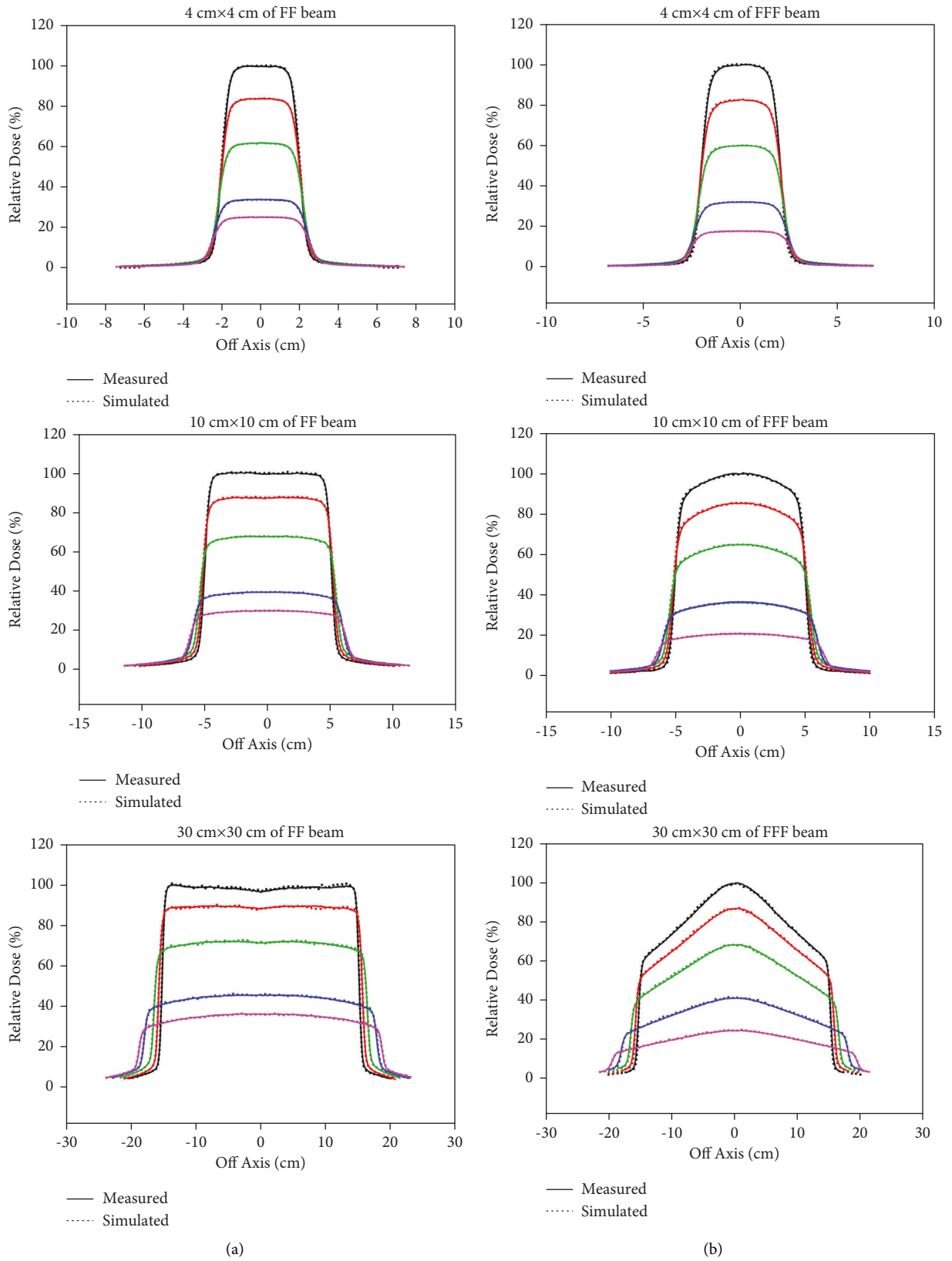


FIGURE 9: The comparison of measured and simulated off-axis dose curves for  $4 \times 4$ ,  $10 \times 10$ ,  $30 \times 30$  cm<sup>2</sup> field sizes at various depths (the depths of FF beams in (a) from top to bottom are,  $d_{max}$ , 5, 10, 20, 25 cm and the depths of FFF beams in (b) from top to bottom are,  $d_{max}$ , 5, 10, 20, 30 cm). Solid lines represent measured data and dotted lines represent simulated data.

TABLE 4: Gamma passing rates of off-axis dose curves for different field sizes ( $\text{cm}^2$ ) at 10 cm depth in FF mode and FFF mode when the gamma criteria is 1 mm/1% (local dose).

Field size ( $\text{cm}^2$ )	FF (%)	FFF (%)
$4 \times 4$	100	100
$6 \times 6$	100	100
$8 \times 8$	100	100
$10 \times 10$	100	100
$15 \times 15$	100	100
$20 \times 20$	99.3	100
$25 \times 25$	99.6	97.0
$30 \times 30$	99.4	97.3

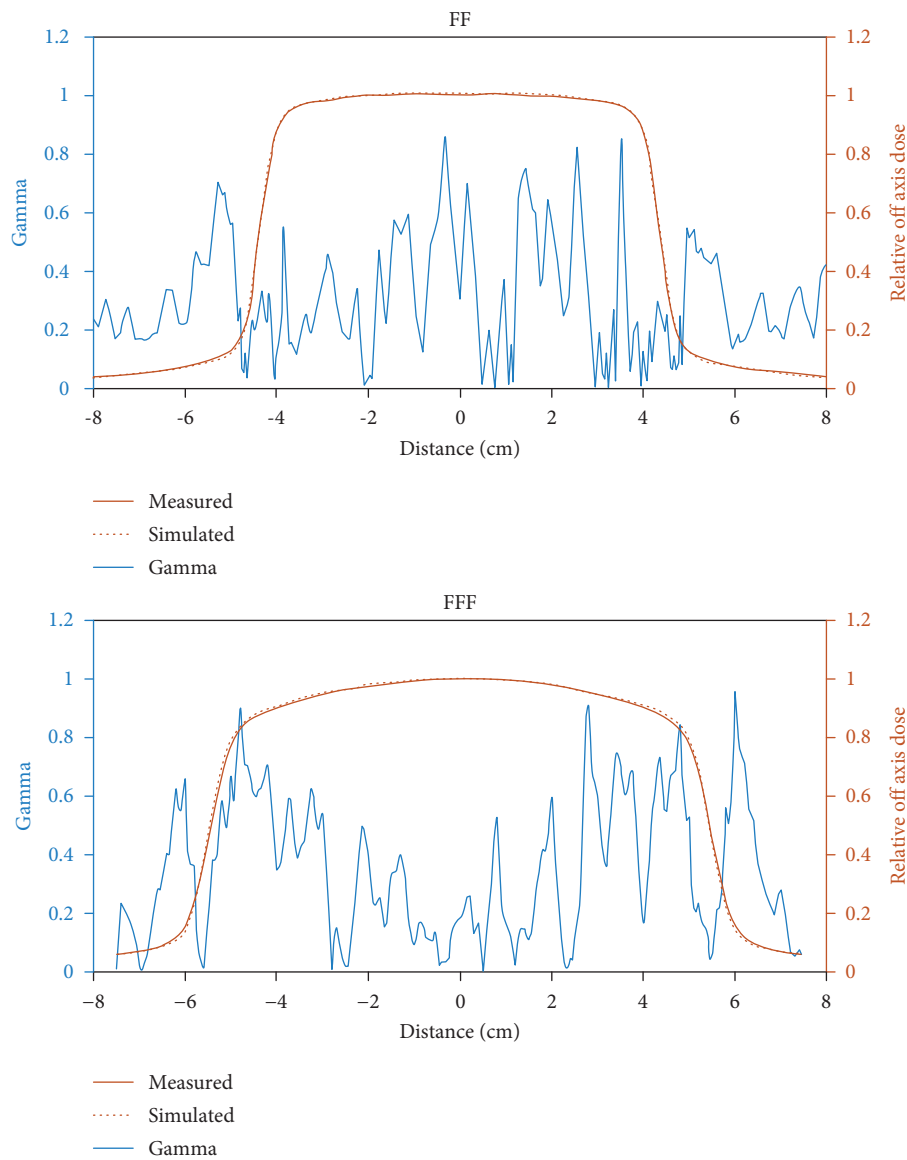


FIGURE 10: The gamma analysis results of measured and simulated off-axis doses produced by FF and FFF beams for  $10 \times 10 \text{ cm}^2$  field at 10 cm depth (Distance-To-Agreement: 1 mm, Dose Difference: 1%). The blue curve represents the gamma value; the solid red line represents the measured off-axis dose; and the dotted red line represents the simulated off-axis dose.

TABLE 5: The simulated and measured profiles of penumbras (cm) of FF and FFF beams for different fields at 10 cm depth (The uncertainties of simulated penumbras in FF mode of  $4 \times 4$ ,  $6 \times 6$ ,  $8 \times 8$ ,  $10 \times 10$ ,  $15 \times 15$ ,  $20 \times 20$ ,  $25 \times 25$ ,  $30 \times 30$  cm<sup>2</sup> fields were as follows: 0.4%, 0.8%, 0.6%, 0.8%, 1.2%, 1.6%, 1.8%, 2% ( $k=2$ ). The uncertainties of simulated penumbras in FFF mode of  $4 \times 4$ ,  $6 \times 6$ ,  $8 \times 8$ ,  $10 \times 10$ ,  $15 \times 15$ ,  $20 \times 20$ ,  $25 \times 25$ ,  $30 \times 30$  cm<sup>2</sup> fields were as follows: 0.8%, 0.5%, 0.6%, 0.8%, 1%, 1.2%, 1.4%, 1.6% ( $k=2$ )).

Field size (cm <sup>2</sup> )	FF			FFF		
	Simulated (cm)	Measured (cm)	Diff. (%)	Simulated (cm)	Measured (cm)	Diff. (%)
$4 \times 4$	0.646	0.649	-0.462	0.639	0.645	-0.930
$6 \times 6$	0.676	0.673	0.446	0.657	0.672	-2.23
$8 \times 8$	0.711	0.716	-0.698	0.702	0.711	-1.27
$10 \times 10$	0.748	0.752	-0.532	0.741	0.752	-1.46
$15 \times 15$	0.812	0.808	0.495	0.795	0.804	-1.12
$20 \times 20$	0.853	0.867	-1.61	0.845	0.866	-2.42
$25 \times 25$	0.874	0.913	-4.27	0.873	0.902	-3.22
$30 \times 30$	0.990	0.991	-0.100	0.940	0.958	-1.88

TABLE 6: The simulated and measured  $S_{c,p}$  values for various field sizes at the depth of  $d_{max}$  for FF and FFF beams. (The uncertainties of simulated  $S_{c,p}$  values in FF mode of  $4 \times 4$ ,  $6 \times 6$ ,  $8 \times 8$ ,  $10 \times 10$ ,  $15 \times 15$ ,  $20 \times 20$ ,  $25 \times 25$ ,  $30 \times 30$  cm<sup>2</sup> fields were as follows: 0.3%, 0.3%, 0.4%, 0.4%, 0.5%, 0.7%, 0.8%, 1% ( $k=2$ ). The uncertainties of simulated  $S_{c,p}$  values in FFF mode of  $4 \times 4$ ,  $6 \times 6$ ,  $8 \times 8$ ,  $10 \times 10$ ,  $15 \times 15$ ,  $20 \times 20$ ,  $25 \times 25$ ,  $30 \times 30$  cm<sup>2</sup> fields were as follows: 0.3%, 0.3%, 0.4%, 0.4%, 0.5%, 0.6%, 0.6%, 0.8% ( $k=2$ )).

Field size (cm <sup>2</sup> )	FF			FFF		
	Simulated	Measured	Diff. (%)	Simulated	Measured	Diff. (%)
$4 \times 4$	0.932	0.933	-0.107	0.951	0.953	-0.210
$6 \times 6$	0.963	0.962	0.104	0.977	0.976	0.102
$8 \times 8$	0.977	0.984	-0.711	0.987	0.987	0.00
$10 \times 10$	1.00	1.00	—	1.00	1.00	—
$15 \times 15$	1.02	1.03	-0.971	1.03	1.02	0.980
$20 \times 20$	1.05	1.04	0.962	1.04	1.04	0.00
$25 \times 25$	1.06	1.06	-0.00	1.06	1.05	0.952
$30 \times 30$	1.07	1.06	0.943	1.07	1.06	0.943

TABLE 7: The measured and calculated data of flatness and symmetry of FF beams. (The uncertainties of simulated flatness in FF mode of  $4 \times 4$ ,  $6 \times 6$ ,  $8 \times 8$ ,  $10 \times 10$ ,  $15 \times 15$ ,  $20 \times 20$ ,  $25 \times 25$ ,  $30 \times 30$  cm<sup>2</sup> fields were as follows: 0.4%, 0.6%, 0.7%, 0.9%, 1.2%, 1.4%, 1.6%, 2% ( $k=2$ ). The uncertainties of simulated symmetry in FF mode of  $4 \times 4$ ,  $6 \times 6$ ,  $8 \times 8$ ,  $10 \times 10$ ,  $15 \times 15$ ,  $20 \times 20$ ,  $25 \times 25$ ,  $30 \times 30$  cm<sup>2</sup> fields were as follows: 0.3%, 0.4%, 0.5%, 0.6%, 0.8%, 0.9%, 1%, 1.2% ( $k=2$ )).

Field size (cm <sup>2</sup> )	Flatness (%)		Symmetry (%)	
	Simulated (%)	Measured (%)	Simulated (%)	Measured (%)
$4 \times 4$	1.77	2.66	0.0421	0.611
$6 \times 6$	1.82	2.26	0.0453	0.166
$8 \times 8$	1.57	1.80	0.160	0.143
$10 \times 10$	1.49	1.66	0.100	0.127
$15 \times 15$	2.02	1.95	0.110	0.00298
$20 \times 20$	2.16	1.47	0.130	0.0303
$25 \times 25$	2.25	1.66	0.304	0.598
$30 \times 30$	2.33	1.57	0.208	0.626

measured  $S_{c,p}$  values of the largest to the smallest field size was 1.141 and the ratio for FFF beams was 1.108, which were similar to the results demonstrated in the literature by Cashmore [26].

**3.2.6. Flatness and Symmetry.** Table 7 shows the measured and calculated parameters of flatness and symmetry of FF beams for different fields, which were all controlled within 3% and had remarkable orthogonality and symmetry, in accordance with the standards of the International Electrotechnics Commission (IEC) [27].

## 4. Conclusions

In this study, the head unit and initial electron beam of the XHA600D accelerator were modeled accurately using the Monte Carlo-based EGSnrc code system. For accurate Monte Carlo modeling in radiotherapy, it is necessary to precisely define not only the head component of the linear accelerator but also the mean energy, energy spread, radial intensity distribution, and angular divergency of incident electrons. We investigated the effects of different incident parameters on dose distribution PDDs and OARs in the cases of  $4 \times 4$ ,  $10 \times 10$ , and  $30 \times 30$  cm<sup>2</sup> which can represent small, reference

and large fields. We came to the following conclusions: PDD is only affected by mean energy; OAR is greatly affected by the radial intensity distribution, so it can be determined by matching the penumbra width between simulation and measurement. The angular divergency has little effect on OAR for small fields, but has a greater impact on OAR for large field. The effect of energy spread on PDD and OAR is not significant, so this parameter can be ignored when performing Monte Carlo simulations. The incident electron parameters of the nominal 6 MV photon beam were adjusted, and the details of the benchmarking process to obtain accurate incident electron information of the XHA600D accelerator were presented. It was observed that the 6 MeV monoenergetic electron beam with a radial intensity FWHM of 2.5 mm and an angular divergency of  $0.15^\circ$  could accomplish best-fitting of the simulated and measured PDDs and OARs. The obtained reasonable parameters were applied to different fields to evaluate FF and FFF beams of the XHA600D accelerator with PDD, OAR, gamma passing rate, beam quality, total scatter factor, penumbra width, flatness, and symmetry. Whether the degree of agreement between calculated and experimental values or the dosimetric discrepancy between FF and FFF modes, all complied with international dosimetry assessment criteria. Overall, the dosimetric performance of the XHA600D accelerator was fully evaluated, and the accuracy of the Monte Carlo model established in this paper was verified. The incident electron parameters obtained in this paper provide basic data for the establishment of the TPS dose calculation model of the XHAD600 accelerator. This paper lays a foundation for further research on the FFF beam of the XHA600D accelerator in the future, and also provides a certain reference value for other studies to establish an accurate Monte Carlo model.

## Data Availability

The data used to support the findings of this study are included within the article.

## Conflicts of Interest

The authors declare that they have no known competing financial interests or personal relationships that could have appeared to influence the work reported in this paper.

## Acknowledgments

This work was supported by the National Key Research and Development Programme of China (grant no. 2016YFC0105103). The author sincerely thanks all the teachers and schoolmates who helped in the process of this article in Sichuan University, Sichuan Academy of Medical Sciences & Sichuan Provincial People's Hospital and West China Hospital.

## References

- [1] C. M. Ma and S. B. Jiang, "Monte Carlo modelling of electron beams from medical accelerators," *Physics in Medicine and Biology*, vol. 44, no. 12, pp. R157–R189, 1999.
- [2] P. J. Keall, J. V. Siebers, M. Arnfield, J. O. Kim, and R. Mohan, "Monte Carlo dose calculations for dynamic IMRT treatments," *Physics in Medicine and Biology*, vol. 46, no. 4, pp. 929–941, 2001.
- [3] E. Gundem and B. Dirican, "Analysis of characteristics and validation of 6 MV photon beam produced by Elekta Synergy linear accelerator using EGSnrc Monte Carlo code," *Radiation Physics and Chemistry*, vol. 184, Article ID 109491, 2021.
- [4] S. S. Almberg, J. Frengen, A. Kylling, and T. Lindmo, "Monte Carlo linear accelerator simulation of megavoltage photon beams: independent determination of initial beam parameters," *Medical Physics*, vol. 39, no. 1, pp. 40–47, 2011.
- [5] P. Bjork, T. Knoos, and P. Nilsson, "Influence of initial electron beam characteristics on Monte Carlo calculated absorbed dose distributions for linear accelerator electron beams," *Physics in Medicine and Biology*, vol. 47, no. 22, pp. 4019–4041, 2002.
- [6] M. Bencheikh, A. Maghnoouj, J. Tajmouati, A. Didi, and A. O. Ezzati, "Validation of Monte Carlo simulation of 6 MV photon beam produced by varian clinac 2100 linear accelerator using BEAMnrc code and DOSXYZnrc code," *Physics of Particles and Nuclei Letters*, vol. 14, no. 5, pp. 780–787, 2017.
- [7] Z. Feng, H. Yue, Y. Zhang, H. Wu, J. Cheng, and X. Su, "Monte Carlo simulation of beam characteristics from small fields based on truebeam flattening-filter-free mode," *Radiation Oncology*, vol. 11, no. 1, p. 30, 2016.
- [8] J. Deng, S. B. Jiang, A. Kapur, J. S. Li, T. Pawlicki, and C. M. Ma, "Photon beam characterization and modelling for Monte Carlo treatment planning," *Physics in Medicine and Biology*, vol. 45, no. 2, pp. 411–427, 2000.
- [9] G. X. Ding, "Energy spectra, angular spread, fluence profiles and dose distributions of 6 and 18 MV photon beams: results of Monte Carlo simulations for a varian 2100EX accelerator," *Physics in Medicine and Biology*, vol. 47, no. 7, pp. 1025–1046, 2002.
- [10] M. Najafzadeh, M. Hoseini-Ghafarokhi, R. S. M. Bolagh et al., "Benchmarking of Monte Carlo model of siemens oncor® linear accelerator for 18 MV photon beam: determination of initial electron beam parameters," *Journal of X-Ray Science and Technology*, vol. 27, no. 6, pp. 1047–1070, 2020.
- [11] T. Tugrul and O. Erogul, "Determination of initial electron parameters by means of Monte Carlo simulations for the siemens artiste linac 6 MV photon beam," *Reports of Practical Oncology and Radiotherapy*, vol. 24, no. 4, pp. 331–337, 2019.
- [12] Y. Xiao, S. F. Kry, R. Popple et al., "Flattening filter-free accelerators: a report from the AAPM therapy emerging technology assessment work group," *Journal of Applied Clinical Medical Physics*, vol. 16, no. 3, pp. 12–29, 2015.
- [13] S. Sangeetha and C. S. Sureka, "Comparison of flattening filter (FF) and flattening-filter-free (FFF) 6 MV photon beam characteristics for small field dosimetry using EGSnrc Monte Carlo code," *Radiation Physics and Chemistry*, vol. 135, pp. 63–75, 2017.
- [14] A. Asadi, S. K. Razavi-Ratki, K. Jabbari, M. Najafzadeh, and A. Nickfarjam, "Monte Carlo evaluation of the potential benefits of flattening filter free beams from the Onconor® clinical linear accelerator," *Journal of X-Ray Science and Technology*, vol. 26, no. 2, pp. 281–302, 2018.
- [15] I. Kawrakow, E. Mainegra-Hing, D. W. O. Rogers, F. Tessier, and B. R. B. Walters, *The EGSnrc Code System: Monte Carlo Simulation of Electron and Photon Transport*, NRCC Report PIRS-701, National Research Council of Canada, Ontario, Canada, 2020.

- [16] D. W. O. Rogers, B. R. B. Walters, and I. Kawrakow, *BEAMnrc Users Manual*, NRCC Report PIRS-0509(A)revL, National Research Council of Canada, Ontario, Canada, 2021.
- [17] D. Sheikh-Bagheri, D. W. O. Rogers, C. K. Ross, and J. P. Seuntjens, "Comparison of measured and Monte Carlo calculated dose distributions from the NRC linac," *Medical Physics*, vol. 27, no. 10, pp. 2256–2266, 2000.
- [18] I. Kawrakow, D. W. O. Rogers, and B. R. B. Walters, "Large efficiency improvements in BEAMnrc using directional bremsstrahlung splitting," *Medical Physics*, vol. 31, no. 10, pp. 2883–2898, 2004.
- [19] B. R. B. Walters, I. Kawrakow, and D. W. O. Rogers, *DOSXYZnrc Users Manual*, NRCC Report PIRS-794revB, National Research Council of Canada, Ontario, Canada, 2021.
- [20] T. Depuydt, A. Van Esch, and D. P. Huyskens, "A quantitative evaluation of IMRT dose distributions: refinement and clinical assessment of the gamma evaluation," *Radiotherapy & Oncology*, vol. 62, no. 3, pp. 309–319, 2002.
- [21] A. Fogliata, R. Garcia, T. Knoos et al., "Definition of parameters for quality assurance of flattening filter free (FFF) photon beams in radiation therapy," *Medical Physics*, vol. 39, no. 10, pp. 6455–6464, 2012.
- [22] T. C. F. Fonseca, B. M. Mendes, M. A. S. Lacerda et al., "MCMEG: simulations of both PDD and TPR for 6 MV LINAC photon beam using different MC codes," *Radiation Physics and Chemistry*, vol. 140, pp. 386–391, 2017.
- [23] W. Ningyu, G. Shaoxian, C. Fengjie et al., "The study of incident electron parameters of XHA600D medical linear accelerator based on Monte Carlo method," *Nuclear Physics Review*, In press.
- [24] S. Y. Lin, T. C. Chu, and J. P. Lin, "Monte Carlo simulation of a clinical linear accelerator," *Applied Radiation and Isotopes*, vol. 55, no. 6, pp. 759–765, 2001.
- [25] D. Georg, S. Af Wetterstedt, G. Kragl et al., "Dosimetric characteristics of 6 and 10 MV unflattened photon beams," *Radiotherapy & Oncology*, vol. 92, no. 1, pp. S111–S146, 2009.
- [26] J. Cashmore, "The characterization of unflattened photon beams from a 6 MV linear accelerator," *Physics in Medicine and Biology*, vol. 53, no. 7, pp. 1933–1946, 2008.
- [27] International Electrotechnical Commission, *Medical Electrical Equipment—Medical Electron Accelerators—Guidelines for Functional Performance Characteristics*, International Electrotechnical Commission, Geneva, Switzerland, 2008.